Engineering 56 (2026) 120–129

Contents lists available at ScienceDirect

Engineering

journal homepage: www.elsevier.com/locate/eng

Research
6G: From Theory to Practice—Article

A Wideband Amplifying and Filtering Reconfigurable Intelligent Surface for Wireless Relay

Lijie Wu [a,#], Qun Yan Zhou [a,#], Jun Yan Dai [a,b,c,#,*], Siran Wang [a,d,#], Junwei Zhang [a], Zhen Jie Qi [a], Hanqing Yang [a], Ruizhe Jiang [a], Zheng Xing Wang [a], Huidong Li [a], Zhen Zhang [f], Jiang Luo [g], Qiang Cheng [a,b,c,*], Tie Jun Cui [a,b,e,*]

[a] State Key Laboratory of Millimeter Waves, Southeast University, Nanjing 210096, China
[b] Institute of Electromagnetic Space, Southeast University, Nanjing 210096, China
[c] Frontiers Science Center for Mobile Information Communication and Security, Southeast University, Nanjing 210096, China
[d] State Key Laboratory of Terahertz and Millimeter Waves, City University of Hong Kong, Hong Kong 999077, China
[e] Suzhou Laboratory, Suzhou 215000, China
[f] School of Electronics and Communication Engineering, Guangzhou University, Guangzhou 510006, China
[g] School of Electronics and Information, Hangzhou Dianzi University, Hangzhou 310018, China

ARTICLE INFO

Article history:
Received 14 November 2024
Revised 4 June 2025
Accepted 11 June 2025
Available online 19 June 2025

Keywords:
Reconfigurable intelligent surface
Programmable metasurface
Wireless relay
Signal filtering
Signal energy enhancement

ABSTRACT

Programmable metasurfaces have garnered significant attention due to their exceptional ability to manipulate electromagnetic (EM) waves in real time, propelling the emergence of reconfigurable intelligent surfaces (RISs) as a transformative advancement in wireless communication for controlling signal propagation and coverage. However, conventional RISs often suffer from a limited operational range and spectral interference, hindering their practical deployment in wireless relay and communication systems. To overcome this limitation, we propose an amplifying and filtering RIS (AF-RIS) to enhance the in-band signal energy and filter the out-of-band signal of the incident EM waves, thereby achieving RIS array miniaturization and improved anti-interference capability. Furthermore, each AF-RIS element features 2-bit phase control, significantly improving the array's beamforming performance. A meticulously designed 4×8 AF-RIS array is presented by integrating the power dividing and combining networks, which substantially reduces the number of amplifiers and filters, drastically decreasing the hardware costs and power consumption. The experimental results demonstrate the powerful capabilities of the AF-RIS in beam-steering, frequency selectivity, and signal amplification. Thus, the proposed AF-RIS offers significant potential for critical wireless relay applications by improving frequency selectivity, expanding signal coverage, and minimizing hardware size.

© 2025 THE AUTHORS. Published by Elsevier LTD on behalf of Chinese Academy of Engineering and Higher Education Press Limited Company. This is an open access article under the CC BY license (http://creativecommons.org/licenses/by/4.0/).

1. Introduction

In recent years, fifth-generation (5G) networks have been deployed in over ten countries, prompting researchers to increasingly shift focus toward sixth-generation (6G) networks [1–6]. Owing to the proliferation of ubiquitous wireless connectivity enabled by Internet of Things (IoT) technology, there is a substantial demand for higher system capacity in 6G networks [7–10]. Meanwhile, the increasing number of access devices has led to urgent challenges in increasing signal strength, ensuring communication quality, and reducing energy consumption. Among the potential 6G technology solutions, the ultra-massive multiple-input multiple-output (MIMO) system can utilize a high-gain antenna array to increase the signal strength within cellular coverage [11–15]. However, obstructions such as buildings and vegetation still create blind zones in cell areas, affecting users' smooth experience. To solve this problem, repeaters, relays, and other wireless devices are introduced to increase the signal strength in blind zones in order to improve the communication quality [16,17]. Nevertheless, traditional relay systems are increasingly inadequate for 6G requirements due to their high cost, energy

* Corresponding authors.
E-mail addresses: junyand@seu.edu.cn (J.Y. Dai), qiangcheng@seu.edu.cn (Q. Cheng), tjcui@seu.edu.cn (T.J. Cui).
# These authors contributed equally to this work.

https://doi.org/10.1016/j.eng.2025.06.015
2095-8099/© 2025 THE AUTHORS. Published by Elsevier LTD on behalf of Chinese Academy of Engineering and Higher Education Press Limited Company.
This is an open access article under the CC BY license (http://creativecommons.org/licenses/by/4.0/).

demands, and architectural complexity [18,19]. While repeaters are more cost-effective, their inability to achieve beamforming and their omnidirectional coverage often exacerbates intra-cell interference, complicating network planning.

To address these challenges, programmable metasurfaces, also known as reconfigurable intelligent surfaces (RISs) in the communication community, have attracted significant interest due to their distinct advantages of low cost, energy efficiency, and architectural simplicity. A programmable metasurface or RIS typically comprises an array of meticulously designed periodic structures integrated with tunable elements such as positive–intrinsic–negative (PIN) diodes and varactor diodes. By dynamically controlling the tunable elements via a micro-control unit (MCU) or field-programmable gate array (FPGA), the programmable metasurface can achieve real-time control of all fundamental characteristics of electromagnetic (EM) waves, including amplitude, phase, polarization, frequency, and wavevector [20–28].

Leveraging their exceptional manipulation capabilities, programmable metasurfaces have been extensively studied for creating flexibly controlled EM environments, enabling the groundbreaking reconfiguration of wireless channels as RISs [29–32]. Programmable metasurfaces and RISs play a pivotal role in the realm of wireless communications, such as simplified transmitter architectures [33–40] and innovative wireless relays [41–44]. In particular, RISs can be strategically deployed in both indoor and outdoor environments and seamlessly integrated with existing infrastructure to optimize wireless channels collaboratively [45,46]. This integration aims to reshape the wireless environment, thereby increasing the signal-to-noise ratio (SNR) and expanding the signal coverage range [47–49]. Consequently, RISs offer a compelling solution for next-generation 6G systems, delivering simple, high-efficiency wireless relaying and earning recognition as one of the World Economic Forum's top-10 emerging technologies in 2024 [50].

Nevertheless, the effectiveness of this technology is sometimes limited by additional path loss attenuation in the relay links, which results from a significant reduction in scattering energy at the material interface due to the non-negligible loss of the tunable elements in RISs. Consequently, larger RIS arrays are often necessary to boost the array gain for sufficient signal strength, resulting in increased hardware costs. To mitigate this problem, programmable metasurfaces with EM wave-amplification functions or amplifying RISs (A-RISs) have emerged as a potential solution. As indicated in Refs. [51–54], the introduction of A-RISs to compensate for path loss yields substantial improvements in energy efficiency, sum-rate gain, and signal coverage in metasurface-aided systems. However, the cited papers predominantly focus on proposing theoretical models of A-RISs and conducting numerical analyses of system performance, lacking practical and detailed RIS design and verifications. Only Zhang et al. [55] experimentally verified an A-RIS signal model using a fabricated A-RIS element, although its complex design and bulky dimensions severely constrain its real-world applicability.

Typically, an amplifying programmable metasurface or an A-RIS is intricately constructed using design principles derived from amplified reflectarray antennas [56–58]. Simple or complicated amplifier circuits are integrated into the metasurface to realize various remarkable functions such as non-reciprocal scattering [59–61], reflection enhancement [62–65], spatial frequency multiplication [66], simultaneous wireless information and power transfers [67], and the construction of programmable diffractive neural networks [68]. However, most amplifying programmable metasurfaces and A-RISs function in a narrow band or lack phase-tuning capability. In addition, they are typically equipped with an amplifier in each unit, resulting in elevated hardware costs and power demands.

Aside from these problems, potential spectrum pollution should be considered. As analyzed in Refs. [69,70], existing RISs not only manipulate signals within the desired frequency range but also affect signals outside of this range, resulting in substantial network interference or security vulnerabilities. A-RISs even strengthen these undesired signals, which may cause even more severe deterioration of the whole communication system. This absence of frequency selectivity requires urgent attention when deploying RISs or A-RISs in an actual wireless environment, particularly given the increasingly congested spectra. To address this issue, the concept of filtering RISs (F-RISs) has emerged as a promising remedy. As indicated in Refs. [71,72], the proposed F-RISs show superior frequency selection and excellent beam-steering ability. However, they suffer from inherent passband losses due to the lack of signal amplification.

In summary, both A-RISs and F-RISs exhibit inherent limitations that hinder their real-world implementation in 6G wireless relay systems. To solve these problems, we herein combine the merits of A-RISs and F-RISs and propose the concept of the amplifying and filtering RIS (AF-RIS). In this article, an AF-RIS is elaborately designed to achieve substantial in-band energy enhancement and out-of-band signal rejection for incident EM waves. Additionally, 2-bit phase tuning is realized to achieve dynamic beam steering. Furthermore, through the introduction of the power combining and dividing networks, a 4×8 AF-RIS array is constructed with fewer amplifiers and filters, greatly reducing the power consumption and hardware cost. The simulated and measured results are in good agreement, affirming the dynamic energy amplification, frequency selectivity, and beamforming capability of the reflected EM wave. A simple and low-cost AF-RIS-based wireless relay system is further established to demonstrate the operational reliability of the array. Given these advancements, the proposed AF-RIS array is poised to play a pivotal role in next-generation communication technologies and wireless systems.

2. Design of the AF-RIS

Fig. 1 provides a conceptual diagram of the proposed AF-RIS array acting as a novel wireless relay. The AF-RIS array enables EM beamforming, frequency selection, and energy amplification. When deployed on a building, it receives and amplifies signals at target frequencies from the base station (BS) while filtering undesired frequencies, then transmits the refined signals to user equipment (UE). This capability significantly extends the coverage range of wireless networks and improves signal quality, particularly in scenarios where obstacles such as roadside trees, buildings, and vehicles severely obstruct the links between the BS and UEs.

As shown in Figs. 2(a) and (b), the AF-RIS array comprises four AF-RIS subarrays, each consisting of four primary components: top patches, a middle slot plane, microstrip networks, and the bottom ground. For a better illustration of the working mechanism, a detailed view of the slot plane and microstrip networks are presented in Fig. 2(c). Specifically, impinging spatial waves are received by the patches, converted to guided waves through the slots, and injected into the microstrip networks. First, the signals are collected by the power-combining networks. Then, they are transmitted to the filtering and amplifying circuit, which provides excellent out-of-band rejection and in-band energy enhancement. After this, the signals are distributed to each AF-RIS element for phase tuning. Finally, the signals are coupled and converted to spatial waves through the different slots for orthogonal reradiation. More details on the phase tuning, power combining and dividing networks, filtering and amplifying circuit, and design of the AF-RIS element are provided in Appendix A Sections S1–S4. Based on the meticulous design of the geometrical structure, the AF-RIS

Fig. 1. Conceptual diagram of the proposed AF-RIS array acting as a novel relay in wireless communications. f_1, f_2, and f_3: different signal frequencies.

exhibits three main advantages, listed as follows for better illustration.

2.1. Phase-tuning and beam-steering capability

The phase-tuning ability of the AF-RIS is achieved through an integrated 0°–90° phase-shifter and 0°–180° switch within each element. By switching the ON or OFF states of the PIN diodes, signals can traverse different microstrip paths to achieve four reconfigurable states with a 90° interval. To assess the phase-tuning and beam-forming ability of the AF-RIS, full-wave simulations were carried out with CST Microwave Studio (MWS), and a subarray of the AF-RIS is analyzed here. In the phase-tuning simulation, each AF-RIS element of the subarray shares the same phase state; as we change the phase states (S0, S1, S2, and S3) of all the elements simultaneously, different phase responses are obtained (Fig. 2(d)). It can be seen that stable 90° phase differences are exhibited between the curves, which enables good 2-bit phase coding within the passband from 2.8 to 3.2 GHz. By independently controlling the phase state of each element, beam steering on the *yoz* plane is enabled. In the passband, the eight AF-RIS elements of the subarray are encoded with seven different coding sequences as examples. The scattering patterns of the reflected waves at 3 GHz are plotted in Fig. 2(e), showing that the AF-RIS subarray reflects the beams in the directions with angles of ±30°, ±20°, ±10°, and 0°. Additionally, Fig. 2(f) visualizes the beam-steering capability by showing the electric field (E-field) intensity distribution on the *yoz* plane at 3 GHz as the AF-RIS array redirects the incident beams to different angles, which are determined by the coding sequences—that is, the phase distributions on the AF-RIS.

2.2. Amplifying and filtering properties

The AF-RIS exhibits significant in-band energy enhancement and a robust out-of-band rejection performance, due to its integrated amplifying and filtering circuit. For comparison, a lossy RIS is considered here. The structure of the lossy RIS is the same as that of the AF-RIS, except that the amplifying and filtering circuit is replaced by a microstrip line. Through a combination of numerical analysis and full-wave simulation, we can obtain the gains of the AF-RIS and lossy RIS with different steering angles in comparison with a metallic plate of the same size. As shown in Fig. 2(g), when the steering angle varies between 0°, 10°, 20°, and 30°, the gains of the lossy RIS and AF-RIS range from –8.5 to –4.9 dB and 17.2 to 21.1 dB, respectively, within 2.8–3.2 GHz. It can be seen that the AF-RIS shows an energy enhancement of over 20 dB in the passband. In addition, by adjusting the integrated circuit's gain, the AF-RIS enables broad reflection amplitude tuning within the passband (Fig. 2(h)), demonstrating dynamic control of the reflected EM wave amplitudes, rather than fixed-level amplification. Furthermore, as can be seen from the curves in Fig. 2(g), the gain of the AF-RIS exhibits a steeper out-of-band reduction compared with that of the lossy RIS, demonstrating an excellent filtering performance. For a better illustration of this filtering ability, the E-field intensity distribution from 2.6 to 3.4 GHz is displayed in Fig. 2(i). At 2.8, 3.0, and 3.2 GHz, the EM waves are successfully reflected in the expected direction. In contrast, at 2.6 and 3.4 GHz, the excellent rejection performance of the AF-RIS can be observed in the stopbands. These simulation results collectively validate the amplifying and filtering functionality of the proposed AF-RIS, which allows the in-band amplification and out-of-band rejection of EM waves.

2.3. Low hardware cost, low energy consumption, and miniaturization advantages

When deployed in wireless communication systems, the additional path loss in relay links typically necessitates larger RIS arrays to maintain sufficient signal strength, leading to substantial hardware costs. As analyzed in Ref. [73], the received signal power through the reflection of an RIS is proportional to the square of the RIS area. In our design, the proposed AF-RIS can provide an energy enhancement of over 20 dB compared with the lossy RIS of the same size. This implies that, given the same amount of energy at the receiver, the area of the array required for the AF-RIS is one-tenth that of a lossy RIS. Consequently, RIS array miniaturization becomes achievable with the AF-RIS, significantly reducing hardware expenditures while maintaining performance.

In previous designs of A-RISs [59–64], each A-RIS element is integrated with an individual active component (an amplifier or transistor). This fully connected architecture leads to excessive power consumption and elevated hardware costs, which can offset the A-RIS's signal enhancement benefits and limit practical deployment. To solve this problem, the power combining and dividing networks are introduced in our design of the AF-RIS subarray. As shown in Fig. 2(c), eight AF-RIS elements share the same filtering and amplifying circuit, while being able to control their phase shift independently. This sub-connected architecture significantly reduces the number of amplifiers, decreasing the power consumption. As revealed in Ref. [52], researchers have theoretically verified that a sub-connected architecture can achieve substantially higher energy efficiency than a fully connected architecture, albeit with reduced beamforming design flexibility. Moreover, even when compared with the lossy RIS, the power consumption of the AF-RIS is one-third less, given the same amount of energy at the receiver. More details about the power consumption of the AF-RIS are provided in Appendix A Section S5.

3. Fabrication and experimental verification

An array of 1 × 4 AF-RIS subarrays was fabricated; a photograph of the prototype is displayed in Figs. 3(a)–(e). The three dielectric layers of the AF-RIS prototype were individually manufactured using printed circuit board (PCB) technology and assembled using plastic fasteners to stabilize the structure. As shown in Fig. 3(a), the upper patches were etched onto an FR4 substrate, while the slot plane and the microstrip networks were separately etched onto the two sides of a Rogers RO4350B substrate. The ground plane is positioned below the slot plane to eliminate back radiation. Two air layers (7.5 mm and 30 mm thick) are sandwiched between these three layers. The fabricated AF-RIS array measures 550 mm × 360 mm. An expansion area is included alongside the AF-RIS array to facilitate handling and assembly, as shown in Figs.

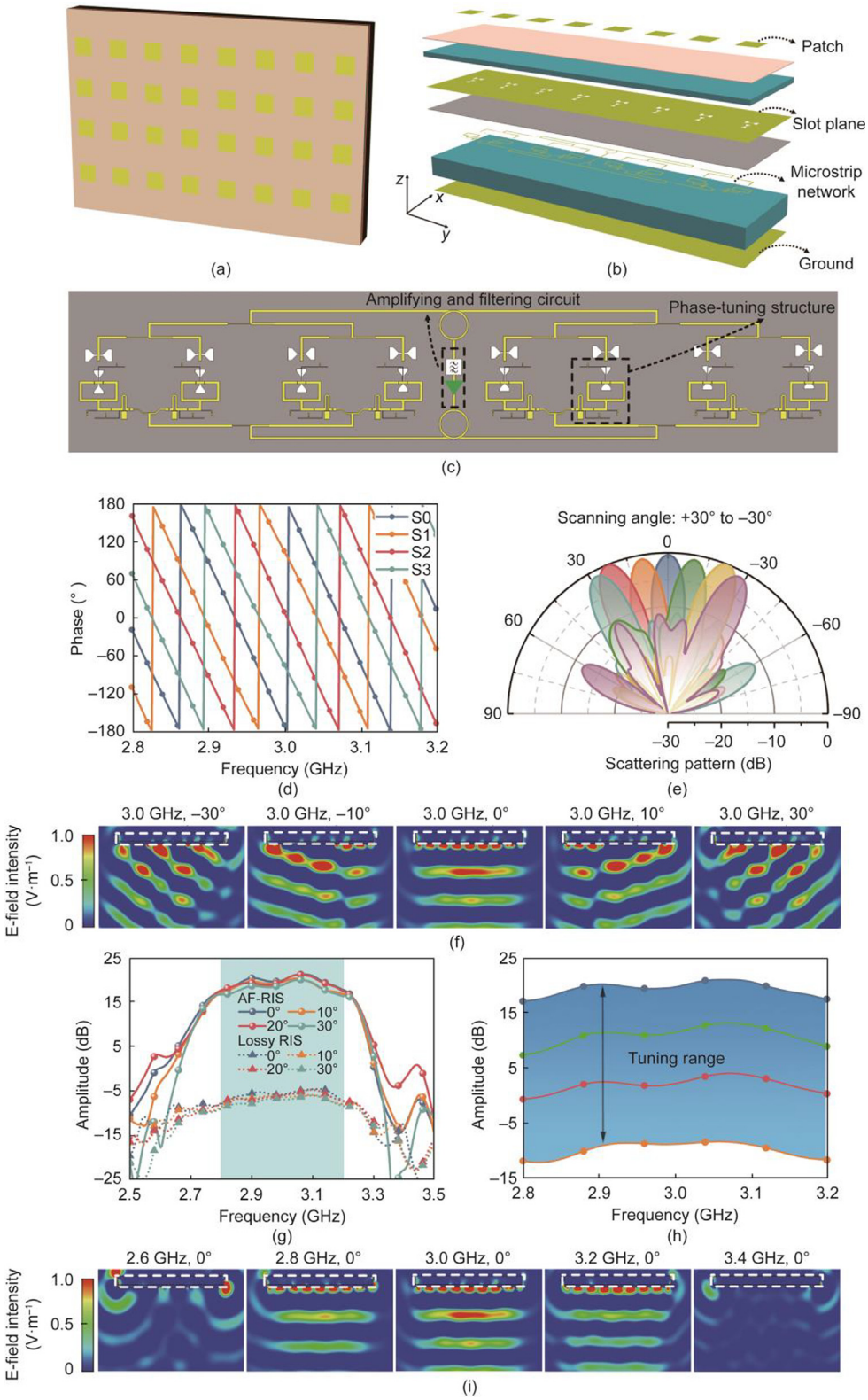

Fig. 2. (a) Front view of the 4 × 8 AF-RIS array. (b) Exploded view of the proposed 1 × 8 AF-RIS subarray. (c) Top view of the slot plane and the microstrip networks of the AF-RIS subarray. (d) Reflection phase response of the AF-RIS subarray across different phase states S0, S1, S2, and S3. (e) Simulated normalized scattering patterns of the passive AF-RIS array. (f) Electric field (E-field) intensity distributions on the *yoz* plane while the reflected beams point in different directions. (g) Reflection amplitude response of the AF-RIS and lossy RIS array under normal incidence, with the reflected beams steering to four different angles. (h) Reflection amplitude of the AF-RIS with wide tuning range in the passband. (i) E-field intensity distributions on the *yoz* plane at different frequencies. *x*, *y*, and *z*: three coordinate axes of the Cartesian coordinate system.

3(b) and (c). A detailed view of the amplifying and filtering circuits and phase-tuning structure is shown in Figs. 3(d) and (e).

The fabricated sample was measured in a basic anechoic environment using the free space method. As shown in Fig. 3(f), two

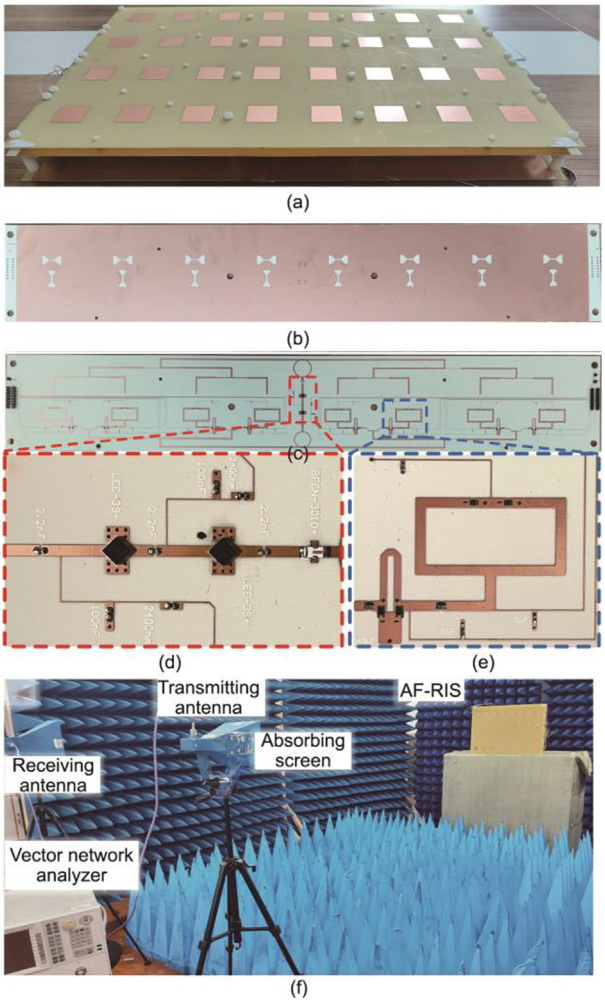

Fig. 3. (a) Prototype of the fabricated AF-RIS array; (b, c) top view of the slot plane and the microstrip networks; (d, e) detailed view of the amplifying and filtering circuit and the phase-tuning structure; (f) photograph of the simple anechoic environment.

horn antennas were connected to a vector network analyzer (Agilent N5245A, Keysight Technologies, USA) to transmit and receive microwave signals. The sample was surrounded by the absorbers to avoid unwanted scattering. The distance between the antennas and the sample was maintained at 5.5 m during the measurement. A direct current (DC) voltage source was connected to the sample to provide the necessary supply voltage. In the measurement, the transmitting antenna was fixed in the normal direction of the sample, while the receiving antenna was positioned in various receiving directions. According to previous discussions, the incident EM wave is received, filtered, amplified, and retransmitted in orthogonal polarization through the AF-RIS array. Thus, the measurement was divided into three steps. First, the receiving antenna was positioned close to the transmitting antenna to ensure that the receiving angle was close to 0°. The two antennas were carefully separated to ensure high isolation between them. The co-reflection coefficients of a metallic control plate of identical size were recorded to calibrate the free space path loss. Then, the receiving antenna was rotated by 90° to obtain the cross-reflection coefficients of the AF-RIS array. Finally, the reflection beam of the AF-RIS array was switched to different directions, and the receiving antenna was adjusted to the corresponding angle to measure the cross-reflection coefficients of the sample. Throughout this movement, the distance between the sample and the receiving antenna remained unchanged to ensure the accuracy of the test. Following these steps, a series of experiments were carried out to validate the AF-RIS's phase-tuning, beam-steering, signal filtering, and amplifying abilities in an indoor anechoic environment, as depicted in Fig. 3(f).

First, the phase-tuning performance of the AF-RIS was validated, and the normalized phase response was measured. In the measurement, all the elements of the AF-RIS array were configured to identical phase states and sequentially cycled through the phase states S0, S1, S2, and S3. As shown in Fig. 4(a), a 2-bit phase-tuning operation with the four reconfigurable coding states was achieved within the passband. Owing to this excellent phase-tuning ability, flexible beam steering can be realized by dynamically changing the coding sequence of the AF-RIS array.

Second, the filtering property of the AF-RIS was validated. After setting the steering beam at 0°, the amplitude responses of the AF-RIS with different control voltages of the amplifying circuit were measured (Fig. 4(b)). It can be seen that the amplitude of the AF-RIS varies at different levels as the control voltage is changed. However, the AF-RIS still exhibits stable and rapid out-of-band amplitude reduction, showing an excellent filtering performance. For a better illustration of the AF-RIS's filtering property, two traditional parameters (the Q factor and the rectangle coefficient K_{20dB}; definitions are provided in Appendix A Section S6) were employed to quantitively measure the filtering property. Typically, the rectangular coefficient K_{20dB} tends to exceed 1, with the optimal value of 1 indicating sharp transitions at both ends of the reflection curve, resulting in an impeccable filtering effect. Hence, an optimal RIS would boast a high Q factor and a K_{20dB} value approaching 1. These two parameters were measured with different control voltages and steering angles, as listed in Figs. 4(c) and (d). The closely clustered values indicate that the AF-RIS shows a stable and excellent filtering effect, ensuring its potential application in various scenarios requiring different beam-steering angles and control voltages.

Finally, the in-band energy enhancement capability of the AF-RIS was determined. The corresponding measured results are presented in Figs. 4(e)–(h). The upper and lower bounds in the figure are the maximum and minimum reflection amplitude of the AF-RIS, while the red dashed line is the reflection amplitude of the AF-RIS with the control voltage setting set to 2 V to mimic the amplitude of a normal lossy RIS. The results indicate that the AF-RIS array dynamically reflects the normal incident EM wave in the directions of 0°, 10°, 20°, and 30° with an energy enhancement of more than 20 dB, compared with the lossy RIS. Also, a minimum amplitude tuning range of 25 dB is realized as the supply voltage is controlled from 1 to 7 V. It should be mentioned that the amplifier's maximum permissible input power is limited to 13 dBm. Additionally, the amplifier's 1 dB compression point is specified as 11.6 dBm at 2 GHz and as 10.1 dBm at 8 GHz. Thus, the output power of the AF-RIS system should ideally be regulated to less than 10 dBm for peak operational efficacy. This power limitation can be optimized through the strategic selection of an alternative amplifier with increased linearity and higher saturation output power.

To better illustrate the novelty and advantages of this work, we compared it with similar studies; the results are summarized in Table 1 [59,62,64,65,67,71,72]. It can be seen that the proposed AF-RIS shows distinctive advantages in bandwidth, amplifying and filtering performance, and beam-scanning range. Moreover, given the introduction of the power dividing and combining networks, the proposed array requires fewer amplifiers compared with other designs.

Overall, the fabricated AF-RIS array demonstrates dynamic phase tuning and beamforming abilities, stable frequency selectivity, commendable energy amplification, and flexible reflection amplitude tuning—characteristics that provide a solid hardware

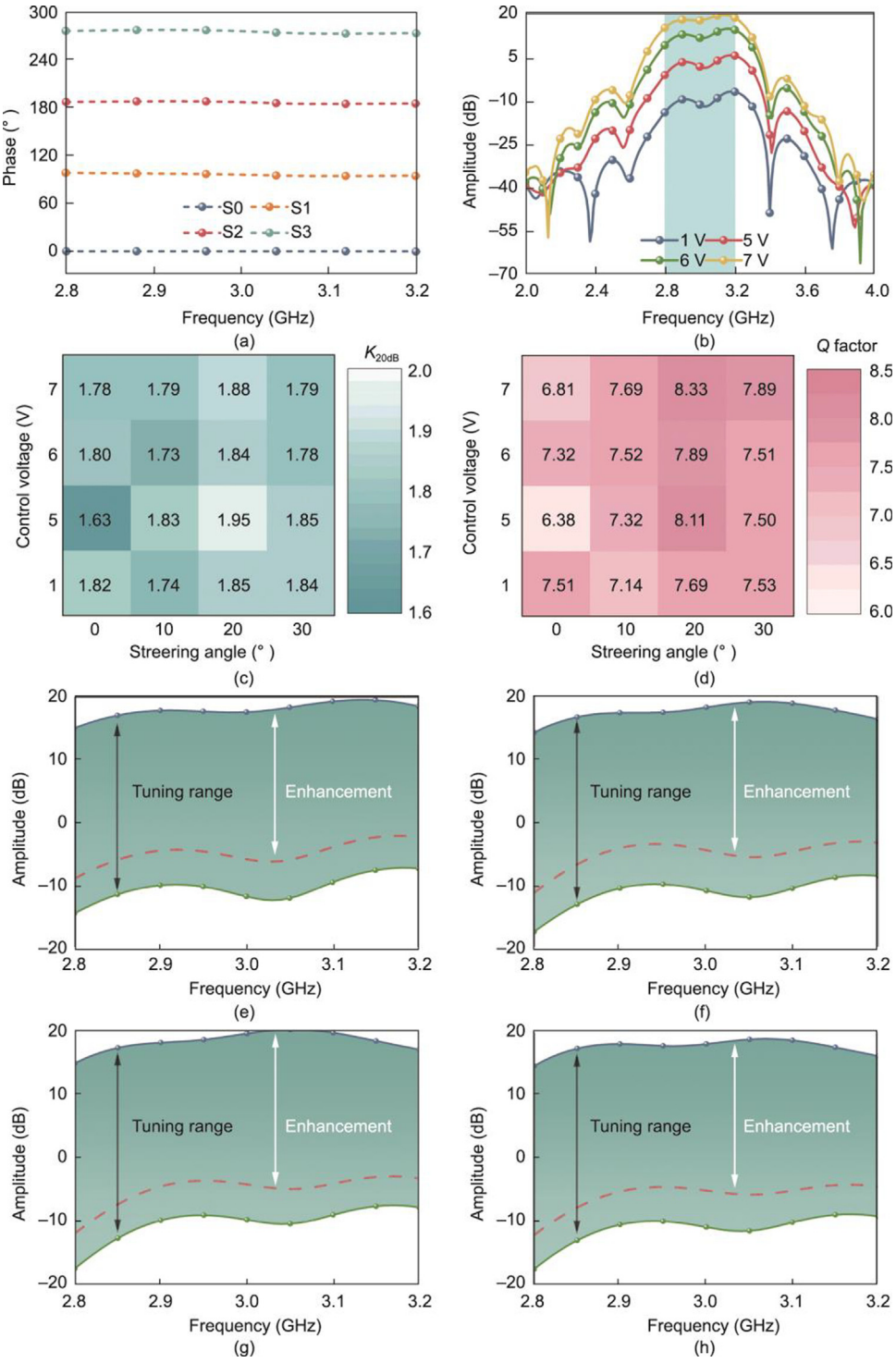

Fig. 4. (a) Normalized phase response of the AF-RIS with the steering angle set as 0° and a control voltage of 7 V. (b) Amplitude response of the AF-RIS with different control voltages with a steering angle of 0°. (c, d) The rectangular coefficient K_{20dB} and the *Q* factor of the AF-RIS with different steering angles and control voltages. (e–h) Amplitude responses of the AF-RIS in the operating bandwidth at different steering angles of (e) θ = 0°, (f) θ = 10°, (g) θ = 20°, and (h) θ = 30°. θ: the steering angle.

foundation for further applications in real wireless communication scenarios. More details about the amplifying and filtering performance of the AF-RIS are provided in Section S6.

4. Validation of AF-RIS-assisted wireless communication

To evaluate the performance improvement enabled by the AF-RIS array in a practical wireless communication system, a series of experiments were conducted using a software-defined radio (SDR) platform (USRP-2974, National Instruments, USA). As shown in Fig. 5, two horn antennas were connected to the SDR platform for signal transmitting and receiving. The AF-RIS array was positioned in the normal direction of the transmitting antenna as the wireless relay, while the receiving antenna was placed at an appropriate receiving angle. The distance between the array and the transmitting/receiving antenna was 6 m. A video source was

Table 1
Function comparison between our design and others in the literature.

Ref.	Frequency (GHz)	Bandwidth	Amplifying performance (dB)	Filtering ability	Beam-scanning range	Number of amplifiers
[59]	5.0	N/A	Maximum 8.4	N/A	−20° to +20°	1/unit
[62]	4.0	7.4%	Maximum 5.8	N/A	N/A	1/unit
[64]	4.0	6.4%	Maximum 5.2	N/A	N/A	1/unit
[65]	5.5	18.2%	Maximum 12.2	N/A	N/A	0.25/unit
[67]	4.0	2.5%	Maximum 12.0	N/A	−30° to +30°	1/unit
[71]	3.5	5.7%	N/A	Yes	−28° to +28°	N/A
[72]	5.1	7.8%	N/A	Yes	0° to +60°	N/A
This work	3.0	12.5%	Maximum 20.0	Yes	−30° to +30°	0.25/unit

N/A: not applicable.

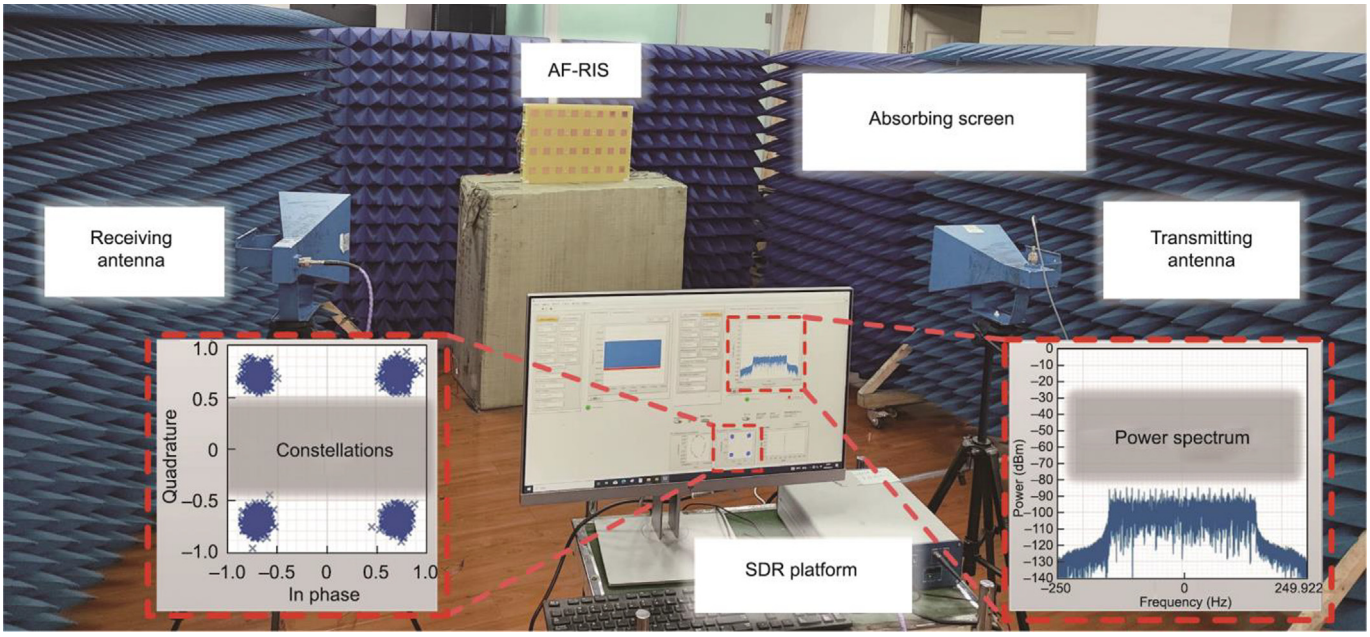

Fig. 5. Photograph of the wireless communication system with the AF-RIS.

encoded into a bitstream, modulated by a quadrature phase-shift keying (QPSK) modulation scheme, transmitted to the AF-RIS array, relayed to the receiving antenna via beamforming, and subsequently demodulated by the SDR platform itself. To illustrate the performance of our AF-RIS array effectively, the energy of the transmitted signal was deliberately constrained to −10 dBm.

Five different cases were designed to showcase the effectiveness of the AF-RIS array, and the corresponding energy spectra and constellation diagrams were measured and obtained (Fig. 6). Table 2 summarizes the settings of the AF-RIS and directions of the receiving antenna. In case 1, the carrier frequency is set at 3 GHz, and the control voltage of the amplifying circuit in the AF-RIS array is set at 2 V, acting as a lossy RIS without energy amplification for a fair comparison. The array is set to reflect the beam in the normal direction, not toward the receiving antenna. As evidenced in Fig. 6(a), the received signal power is very low, the constellation diagram is completely cluttered, and there is no video image on the screen of the receiving terminal, indicating that the information transmission is completely interrupted. In case 2, the control voltage of the amplifiers is unchanged, while the reflected beam of the array is set to point toward the receiving antenna. In this scenario, as shown in Fig. 6(b), the power of the received signal is strengthened, and the constellation diagram is obviously improved. This can be attributed to the gain introduced by the beamforming function of the array. However, the signal transmission still suffers from severe deterioration (i.e., mosaic artifacts in the received video). In this case, the energy of the transmitted signal is set at a low level, as mentioned above, which means that the extra gain of the beamforming function is insufficient to provide adequate signal energy enhancement to improve the communication quality. Thus, further in-band signal energy enhancement is considered in case 3, where the control voltage of the amplifying circuit is switched to 7 V, indicating significant energy amplification. As shown in Fig. 6(c), the signal power is clearly elevated, leading to a much more cohesive and condensed clustering of constellation points in the QPSK constellation diagram. Moreover, the video is transmitted smoothly without any disruptions, ensuring uninterrupted playback at the receiving end. With the extra energy amplification provided by the AF-RIS array, the communication quality is greatly improved in comparison with cases 1 and 2. Finally, our test verifies the out-of-band signal rejection. In cases 4 and 5, the signal frequency is set at 2.65 and 3.35 GHz, respectively, while the other conditions remain unchanged. The corresponding measured results are illustrated in Figs. 6(d) and (e). As shown in the energy spectra, the energy of the out-of-band signals is successfully suppressed, avoiding potential interference with current wireless communication systems. The worsened constellation diagram and the deterioration of the video transmission also strongly suggest that such signals are rejected by the AF-RIS, indicating its excellent filtering performance.

To perform a quantitative analysis of the signal transmission performance, we analyzed the received SNR relative to the power of the transmitted signal across cases 1–3, as depicted in

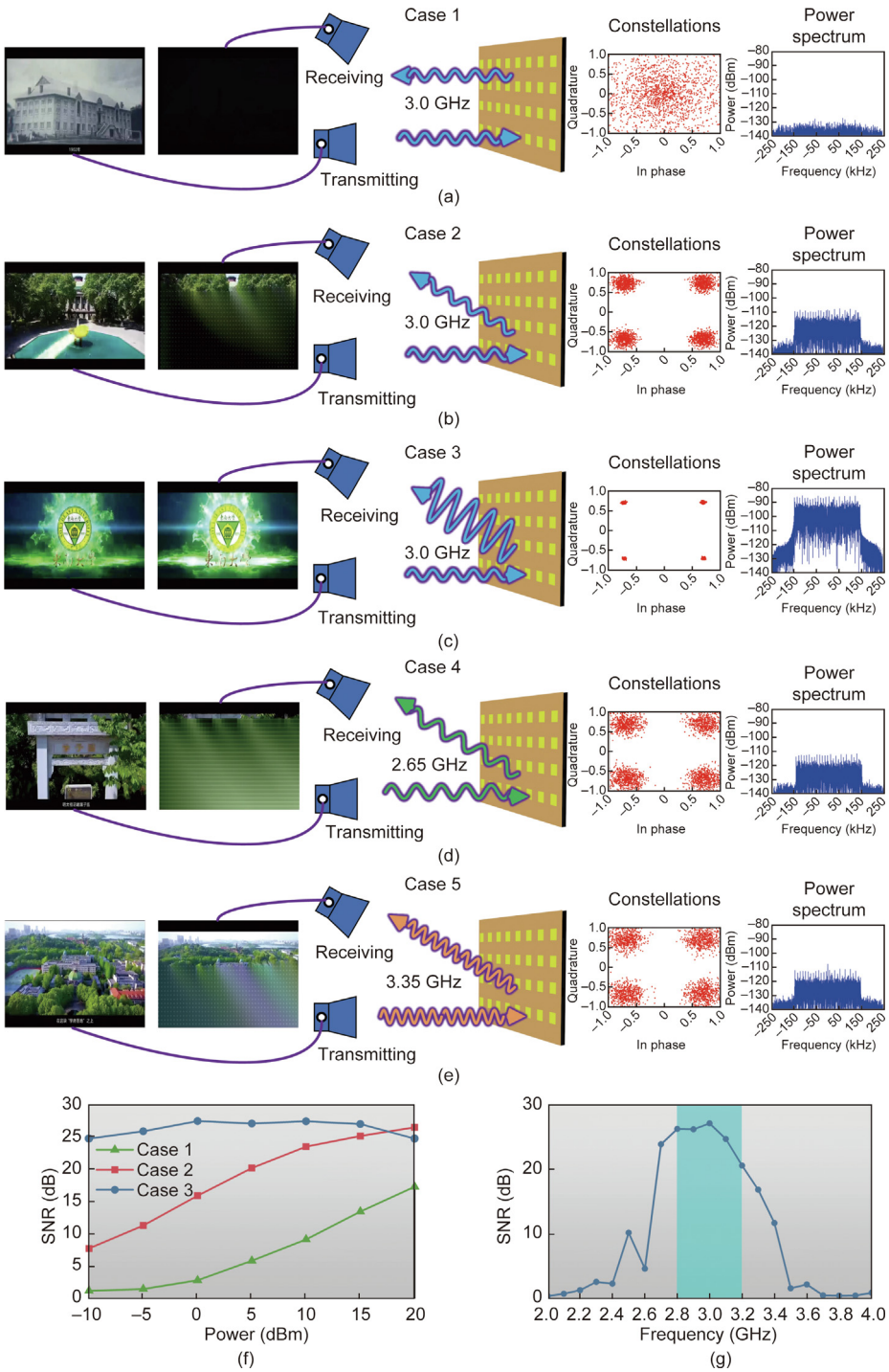

Fig. 6. Wireless communication experiments to demonstrate the energy amplification and frequency filtering of the AF-RIS. (a–e) Five cases with different settings of the AF-RIS and receiving antenna. (f) The SNR spectrum in relation to the power of the transmitted signal in cases 1, 2, and 3. (g) The SNR spectrum in case 3 with a transmitted signal power of −10 dBm.

Table 2
Settings of the AF-RIS and receiving antennas in the wireless communication experiments.

Case	Theoretical beam direction	Receiving antenna direction	Amplifying mode (Yes/No)	Operating frequency (GHz)
1	0°	30°	No	3.00
2	30°	30°	No	3.00
3	30°	30°	Yes	3.00
4	30°	30°	Yes	2.65
5	30°	30°	Yes	3.35

Fig. 6(f). A noticeable trend reveals that, in cases 1 and 2, there is a corresponding incremental improvement in the SNR as the signal power increases; moreover, in case 3, the received SNR becomes relatively stable. This is because, when the transmitter noise is lower than the receiver noise, the received SNR obviously increases with the transmitted power. In contrast, when the transmitter noise prevails in the overall system noise, the SNR will not change dramatically, since the AF-RIS amplifies the signal and noise from the transmitter equally. As analyzed, when the signal power is at a relatively low level, the AF-RIS provides a considerable increase in the SNR compared with the lossy RIS. Fig. 6(g) further shows the received SNR at different carrier frequencies in case 3 with a signal power of –10 dBm. The measured results demonstrate a distinct 27.1 dB peak at 3.0 GHz, with the values are maintained at above 20.5 dB across 2.8–3.2 GHz. Outside the 2.5–3.4 GHz operational band, the SNR plummets to below 11.7 dB, confirming the array's sharp frequency selectivity.

The above discussion suggests that the AF-RIS, acting as a wireless relay, delivers enhanced signal energy, superior frequency selectivity, and improved communication quality compared with the lossy RIS. This methodology offers promising potential for expanding coverage domains, reducing spectral congestion, and optimizing RIS array dimensions.

5. Conclusions

In this work, we presented a novel AF-RIS architecture integrating in-band amplification, out-of-band filtering, and dynamic beam-steering capabilities to improve wireless communication systems. By incorporating dual-polarized slot-coupled patches with an integrated filtering/amplification circuit and phase-tuning structures, an AF-RIS prototype was fabricated and evaluated in a basic anechoic chamber setup. The measurement results demonstrated an in-band gain of 20 dB and significant stopband suppression, closely matching the simulated performance. The integrated 2-bit phase-tuning mechanism enables dynamic manipulation of the wave propagation while maintaining robust filtering/amplification across angular variations. Experimental validation in wireless communication scenarios confirmed the AF-RIS's simultaneous amplification, frequency-selective operation, and beamforming functionalities. The system exhibits a notable relay performance, with low hardware complexity and power demands. It is anticipated that the proposed AF-RIS will be valuable for increasing the signal coverage, alleviating spectrum pollution, and reducing the size of metasurface arrays in 6G wireless communication systems.

CRediT authorship contribution statement

Lijie Wu: Writing – review & editing, Writing – original draft, Validation, Methodology, Data curation. **Qun Yan Zhou:** Writing – review & editing, Validation, Methodology. **Jun Yan Dai:** Writing – review & editing, Project administration, Funding acquisition. **Siran Wang:** Writing – review & editing, Validation, Methodology. **Junwei Zhang:** Validation, Investigation. **Zhen Jie Qi:** Writing – review & editing, Validation, Investigation. **Hanqing Yang:** Validation, Investigation. **Ruizhe Jiang:** Validation, Investigation. **Zheng Xing Wang:** Validation, Investigation. **Huidong Li:** Supervision, Formal analysis. **Zhen Zhang:** Supervision. **Jiang Luo:** Supervision, Formal analysis. **Qiang Cheng:** Writing – review & editing, Methodology, Funding acquisition. **Tie Jun Cui:** Writing – review & editing, Funding acquisition, Conceptualization.

Declaration of competing interest

The authors declare that they have no known competing financial interests or personal relationships that could have appeared to influence the work reported in this paper.

Acknowledgments

This work was supported by the National Key Research and Development Program of China (2023YFB3811502), the National Natural Science Foundation of China (62225108, 62288101, and 62201139), the Jiangsu Province Frontier Leading Technology Basic Research Project (BK20212002), the Jiangsu Provincial Scientific Research Center of Applied Mathematics (BK20233002), the Program of Song Shan Laboratory (included in the management of the Major Science and Technology Program of Henan Province; 221100211300-02 and 221100211300-03), the 111 Project (111-2-05), the Fundamental Research Funds for the Central Universities (2242022k60003, 2242024RCB0005, and 2242024K30009), and the Southeast University–China Mobile Research Institute Joint Innovation Center (R202111101112JZC02).

Appendix A. Supplementary data

Supplementary data to this article can be found online at https://doi.org/10.1016/j.eng.2025.06.015.

References

[1] Alsabah M, Naser M, Mahmmod B, Abdulhussain S, Eissa M, Al-Baidhani A, et al. 6G wireless communications networks: a comprehensive survey. IEEE Access 2021;9:148191–243.
[2] Cui M, Wu Z, Lu Y, Wei X, Dai L. Near-field MIMO communications for 6G: fundamentals, challenges, potentials, and future directions. IEEE Commun Mag 2023;61(1):40–6.
[3] Wang C, You X, Gao X, Zhu X, Li Z, Zhang C, et al. On the road to 6G: visions, requirements, key technologies, and testbeds. IEEE Commun Surv Tutor 2023;25(2):905–74.
[4] Shafie A, Yang N, Han C, Jornet J, Juntti M, Kürner T. Terahertz communications for 6G and beyond wireless networks: challenges, key advancements, and opportunities. IEEE Netw 2023;37(3):162–9.
[5] Zhou D, Sheng M, Li J, Han Z. Aerospace integrated networks innovation for empowering 6G: a survey and future challenges. IEEE Commun Surv Tutor 2023;25(2):975–1019.
[6] Zhang P, Chen N, Shen S, Yu S, Kumar N, Hsu C. AI-enabled space–air–ground integrated networks: management and optimization. IEEE Netw 2024;38(2):186–92.
[7] Qadir Z, Le K, Saeed N, Munawar H. Towards 6G Internet of Things: recent advances, use cases, and open challenges. ICT Express 2023;9(3):296–312.
[8] Malik U, Javed M, Zeadally S, Islam S. Energy-efficient fog computing for 6G-enabled massive IoT: recent trends and future opportunities. IEEE Internet Things J 2022;9(16):14572–94.
[9] Nguyen D, Ding M, Pathirana P, Seneviratne A, Li J, Niyato D, et al. 6G Internet of Things: a comprehensive survey. IEEE Internet Things J 2022;9(1):359–83.
[10] Khalid W, Rehman MAU, Van Chien T, Kaleem Z, Lee H, Yu H. Reconfigurable intelligent surface for physical layer security in 6G–IoT: designs, issues, and advances. IEEE Internet Things J 2024;11(2):3599–613.
[11] Akyildiz I, Jornet J. Realizing ultra-massive MIMO (1024 × 1024) communication in the (0.06–10) terahertz band. Nano Commun Netw 2016;8:46–54.
[12] Liao A, Gao Z, Wang D, Wang H, Yin H, Ng D, et al. Terahertz ultra-massive MIMO-based aeronautical communications in space–air–ground integrated networks. IEEE J Sel Areas Commun 2021;39(6):1741–67.
[13] Yuan Y, He R, Ai B, Ma Z, Miao Y, Niu Y, et al. A 3D geometry-based THz channel model for 6G ultra massive MIMO systems. IEEE Trans Veh Technol 2022;71(3):2251–66.
[14] Deng R, Zhang Y, Zhang H, Di B, Zhang H, Poor H, et al. Reconfigurable holographic surfaces for ultra-massive MIMO in 6G: practical design, optimization and implementation. IEEE J Sel Areas Commun 2023;41(8):2367–79.
[15] Zeng S, Di B, Zhang H, Gao J, Yue S, Hu X, et al. RIS-based IMT-2030 testbed for mmWave multi-stream ultra-massive MIMO communications. IEEE Wirel Commun 2024;31(3):375–82.
[16] Rankov B, Wittneben A. Spectral efficient protocols for half-duplex fading relay channels. IEEE J Sel Areas Commun 2007;25(2):379–89.

[17] Lu W, Di Renzo M. Stochastic geometry modeling and system-level analysis & optimization of relay-aided downlink cellular networks. IEEE Trans Commun 2015;63(11):4063–85.
[18] Rappaport T, Xing Y, Kanhere O, Ju S, Madanayake A, Mandal S, et al. Wireless communications and applications above 100 GHz: opportunities and challenges for 6G and beyond. IEEE Access 2019;7:78729–57.
[19] Di Renzo M, Ntontin K, Song J, Danufane FH, Qian X, Lazarakis F, et al. Reconfigurable intelligent surfaces vs. relaying: differences, similarities, and performance comparison. IEEE Open J Commun Soc 2020;1:798–807.
[20] Cui TJ, Qi MQ, Wan X, Zhao J, Cheng Q. Coding metamaterials, digital metamaterials and programmable metamaterials. Light Sci Appl 2014;3(10):e218.
[21] Cui TJ, Liu S, Zhang L. Information metamaterials and metasurfaces. J Mater Chem C 2017;5(15):3644–68.
[22] Dai JY, Zhao J, Cheng Q, Cui TJ. Independent control of harmonic amplitudes and phases via a time-domain digital coding metasurface. Light Sci Appl 2018;7(1):90.
[23] Zhang L, Wu R, Bai G, Wu H, Ma Q, Chen X, et al. Transmission–reflection-integrated multifunctional coding metasurface for full-space controls of electromagnetic waves. Adv Funct Mater 2018;28(33):1802205.
[24] Zhang L, Chen X, Shao R, Dai J, Cheng Q, Castaldi G, et al. Breaking reciprocity with space–time-coding digital metasurfaces. Adv Mater 2019;31(41):1970295.
[25] Dai JY, Yang J, Tang W, Chen MZ, Ke JC, Cheng Q, et al. Arbitrary manipulations of dual harmonics and their wave behaviors based on space–time-coding digital metasurface. Appl Phys Rev 2020;7(4):041408.
[26] Zhang XG, Sun YL, Yu Q, Cheng Q, Jiang WX, Qiu CW, et al. Smart Doppler cloak operating in broad band and full polarizations. Adv Mater 2021;33(17):2007966.
[27] Wang S, Dai J, Zhou Q, Ke J, Cheng Q, Cui T. Manipulations of multi-frequency waves and signals via multi-partition asynchronous space–time-coding digital metasurface. Nat Commun 2023;14:5377.
[28] Liu W, Wang SR, Dai JY, Zhang L, Chen Q, Cheng Q, et al. Arbitrarily rotating polarization direction and manipulating phases in linear and nonlinear ways using programmable metasurface. Light Sci Appl 2024;13:172.
[29] Wu Q, Zhang R. Towards smart and reconfigurable environment: intelligent reflecting surface aided wireless network. IEEE Commun Mag 2020;58(1):106–12.
[30] Di Renzo M, Zappone A, Debbah M, Alouini MS, Yuen C, de Rosny J, et al. Smart radio environments empowered by reconfigurable intelligent surfaces: how it works, state of research, and the road ahead. IEEE J Sel Areas Commun 2020;38(11):2450–525.
[31] Liu Y, Liu X, Mu X, Hou T, Xu J, Di Renzo M, et al. Reconfigurable intelligent surfaces: principles and opportunities. IEEE Commun Surv Tutor 2021;23(3):1546–77.
[32] Basar E, Di Renzo M, De Rosny J, Debbah M, Alouini MS, Zhang R. Wireless communications through reconfigurable intelligent surfaces. IEEE Access 2019;7:116753–73.
[33] Cui TJ, Liu S, Bai GD, Ma Q. Direct transmission of digital message via programmable coding metasurface. Research 2019;2019:2584509.
[34] Dai J, Tang W, Zhao J, Li X, Cheng Q, Ke J, et al. Wireless communications through a simplified architecture based on time-domain digital coding metasurface. Adv Mater Technol 2019;4(7):1900044.
[35] Tang W, Chen MZ, Dai JY, Zeng Y, Zhao X, Jin S, et al. Wireless communications with programmable metasurface: new paradigms, opportunities, and challenges on transceiver design. IEEE Wirel Commun 2020;27(2):180–7.
[36] Dai JY, Tang W, Yang LX, Li X, Chen MZ, Ke JC, et al. Realization of multi-modulation schemes for wireless communication by time-domain digital coding metasurface. IEEE Trans Antennas Propag 2020;68(3):1618–27.
[37] Zhang L, Chen M, Tang W, Dai J, Miao L, Zhou X, et al. A wireless communication scheme based on space- and frequency-division multiplexing using digital metasurfaces. Nat Electron 2021;4(3):218–27.
[38] Huang C, Zhang J, Cheng Q, Cui T. Polarization modulation for wireless communications based on metasurfaces. Adv Funct Mater 2021;31(36):2103379.
[39] Chen MZ, Tang W, Dai JY, Ke JC, Zhang L, Zhang C, et al. Accurate and broadband manipulations of harmonic amplitudes and phases to reach 256 QAM millimeter-wave wireless communications by time-domain digital coding metasurface. Nat Sci Rev 2022;9(1):nwab134.
[40] Liu Y, Wang Y, Fu X, Shi L, Yang F, Luo J, et al. Toward sub-terahertz: space–time coding metasurface transmitter for wideband wireless communications. Adv Sci 2023;10(29):2304278.
[41] Yildirim I, Kilinc F, Basar E, Alexandropoulos G. Hybrid RIS-empowered reflection and decode-and-forward relaying for coverage extension. IEEE Commun Lett 2021;25(5):1692–6.
[42] Kan T, Chang R, Chien F, Chen B, Poor H. Hybrid relay and reconfigurable intelligent surface assisted multiuser MISO systems. IEEE Trans Veh Technol 2023;72(6):7653–68.
[43] Cheng Y, Li KH, Liu Y, Teh KC, Vincent PH. Downlink and uplink intelligent reflecting surface aided networks: NOMA and OMA. IEEE Trans Wirel Commun 2021;20(6):3988–4000.
[44] Arzykulov S, Nauryzbayev G, Celik A, Eltawil A. RIS-assisted full-duplex relay systems. IEEE Syst J 2022;16(4):5729–40.
[45] Zhu F, Wang X, Huang C, Yang Z, Chen X, Al Hammadi A, et al. Robust beamforming for RIS-aided communications: gradient-based manifold meta learning. IEEE Trans Wirel Commun 2024;23(11):15945–56.
[46] Wang X, Zhu F, Zhou Q, Yu Q, Huang C, Alhammadi A, et al. Energy-efficient beamforming for RISs-aided communications: gradient based meta learning. In: Proceedings of IEEE International Conference on Communications, 2024 Jun 9–13; Denver, CO, USA. New York City: IEEE; 2024. p. 3464–9.
[47] Wang W, Zhang W. Joint beam training and positioning for intelligent reflecting surfaces assisted millimeter wave communications. IEEE Trans Wirel Commun 2021;20(10):6282–97.
[48] Wang J, Liang Y, Joung J, Yuan X, Wang X. Joint beamforming and reconfigurable intelligent surface design for two-way relay networks. IEEE Trans Commun 2021;69(8):5620–33.
[49] Obeed M, Chaaban A. Joint beamforming design for multiuser miso downlink aided by a reconfigurable intelligent surface and a relay. IEEE Trans Wirel Commun 2022;21(10):8216–29.
[50] Top 10 emerging technologies of 2024. Report. Geneva: World Economic Forum; 2024.
[51] Ma Y, Li M, Liu Y, Wu Q, Liu Q. Optimization for reflection and transmission dual-functional active RIS-assisted systems. IEEE Trans Commun 2023;71(9):5534–48.
[52] Liu K, Zhang Z, Dai L, Xu S, Yang F. Active reconfigurable intelligent surface: fully-connected or sub-connected? IEEE Commun Lett 2022;26(1):167–71.
[53] Long R, Liang YC, Pei Y, Larsson EG. Active reconfigurable intelligent surface-aided wireless communications. IEEE Trans Wirel Commun 2021;20(8):4692.
[54] Ma Y, Li M, Liu Y, Wu Q, Liu Q. Active reconfigurable intelligent surface for energy efficiency in MU-MISO systems. IEEE Trans Veh Technol 2023;72(3):4103–7.
[55] Zhang Z, Dai L, Chen X, Liu C, Yang F, Schober R, et al. Active RIS vs. passive RIS: which will prevail in 6G? IEEE Trans Commun 2023;71(3):1707–25.
[56] Bialkowski M, Robinson A, Song H. Design, development, and testing of X-band amplifying reflectarrays. IEEE Trans Antennas Propag 2002;50(8):1065–76.
[57] Kishor K, Hum S. An amplifying reconfigurable reflectarray antenna. IEEE Trans Antennas Propag 2012;60(1):197–205.
[58] Yang X, Xu S, Yang F, Li M, Fang H, Hou Y. A distributed power-amplifying reflectarray antenna for EIRP boost applications. IEEE Antennas Wirel Propag Lett 2017;16:2742–5.
[59] Wang X, Han J, Tian S, Xia D, Li L, Cui TJ. Amplification and manipulation of nonlinear electromagnetic waves and enhanced nonreciprocity using transmissive space–time-coding metasurface. Adv Sci 2022;9(11):2105960.
[60] Ma Q, Chen L, Jing HB, Hong QR, Cui HY, Liu Y, et al. Controllable and programmable nonreciprocity based on detachable digital coding metasurface. Adv Opt Mater 2019;7(24):1901285.
[61] Taravati S, Khan B, Gupta S, Achouri K, Caloz C. Nonreciprocal nongyrotropic magnetless metasurface. IEEE Trans Antennas Propag 2017;65(7):3589–97.
[62] Qiu T, Jia Y, Wang J, Cheng Q, Qu S. Controllable reflection-enhancement metasurfaces via amplification excitation of transistor circuit. IEEE Trans Antennas Propag 2021;69(3):1477–82.
[63] Taravati S, Eleftheriades G. Full-duplex reflective beamsteering metasurface featuring magnetless nonreciprocal amplification. Nat Commun 2021;12:4414.
[64] Yang J, Yang W, Qu K, Zhao J, Jiang T, Chen K, et al. Active polarization-converting metasurface with electrically controlled magnitude amplification. Opt Express 2023;31(18):28979.
[65] Wu L, Lou K, Ke J, Liang J, Luo Z, Dai JY, et al. A wideband amplifying reconfigurable intelligent surface. IEEE Trans Antennas Propag 2022;70(11):10623–31.
[66] Wang H, Li Y, Wang S, Shen J, Li H, Jin S, et al. High-efficiency spatial-wave frequency multiplication using strongly nonlinear metasurface. Adv Sci 2021;8(18):2101212.
[67] Wang X, Han JQ, Li GX, Xia DX, Chang MY, Ma XJ, et al. High-performance cost efficient simultaneous wireless information and power transfers deploying jointly modulated amplifying programmable metasurface. Nat Commun 2023;14:6002.
[68] Liu C, Ma Q, Luo Z, Hong Q, Xiao Q, Zhang H, et al. A programmable diffractive deep neural network based on a digital-coding metasurface array. Nat Electron 2022;5(2):113–22.
[69] Zhao Y, Lv X. Network coexistence analysis of RIS-assisted wireless communications. IEEE Access 2022;10:63442–54.
[70] Zhao Y. Reconfigurable intelligent surfaces for 6G: applications, challenges, and solutions. Front Inf Technol Electron Eng 2023;24(12):1669–88.
[71] Liang JC, Zhang L, Luo Z, Jiang RZ, Cheng ZW, Wang SR, et al. A filtering reconfigurable intelligent surface for interference-free wireless communications. Nat Commun 2024;15:3838.
[72] Hu Q, Yang H, Zeng X, Rao Y, Zhang X. Methodology and design of absorptive filtering reconfigurable intelligent surfaces. IEEE Trans Antennas Propag 2024;72(6):5301–6.
[73] Tang W, Chen MZ, Chen X, Dai JY, Han Y, Di Renzo M, et al. Wireless communications with reconfigurable intelligent surface: path loss modeling and experimental measurement. IEEE Trans Wirel Commun 2021;20(1):421–39.